In-situ investigation of adhesion mechanisms on complex micro-structured biological surfaces

Charchit Kumar, Damien Favier, Thomas Speck, Vincent Le Houerou

In-situ investigation of adhesion mechanisms on complex micro-structured biological surfaces

Charchit Kumar[1,2,3], Damien Favier[2], Thomas Speck[1,3], and Vincent Le Houérou[2,4,]*

[1] Plant Biomechanics Group and Botanic Garden, Faculty of Biology, University of Freiburg, Schänzlestraße 1, 79104 Freiburg, Germany

[2] Institut Charles Sadron, CNRS UPR022, University of Strasbourg, 23 rue du Loess, BP 84047, 67034 Strasbourg Cedex 2, France

[3] Cluster of Excellence *liv*MatS@FIT, Freiburg Center for Interactive Materials and Bioinspired Technologies (FIT), University of Freiburg, Georges-Kohler-Allee 105, 79110 Freiburg, Germany

[4] Laboratoire ICube, CNRS UMR 7357, University of Strasbourg, 72 route du Rhin, BP 315, F-67411 Illkirch cedex, France

Dr. C. Kumar, Prof. T. Speck
Plant Biomechanics Group and Botanic Garden, Faculty of Biology, University of Freiburg, Schänzlestraße 1, 79104 Freiburg, Germany.
Cluster of Excellence *liv*MatS@FIT, Freiburg Center for Interactive Materials and Bioinspired Technologies (FIT), University of Freiburg, Georges-Kohler-Allee 105, 79110 Freiburg, Germany.

Dr. C. Kumar, D. Favier, Prof. V. Le Houérou
Institut Charles Sadron, CNRS UPR022, University of Strasbourg, 23 rue du Loess, BP 84047, 67034 Strasbourg Cedex 2, France.

Prof. V. Le Houérou
Laboratoire ICube, CNRS UMR 7357, University of Strasbourg, 72 route du Rhin, BP 315, F-67411 Illkirch cedex, France.
E-mail: v.lehouerou@unistra.fr

ORCID IDs:
C. Kumar- 0000-0002-6912-3506
T. Speck- 0000-0002-2245-2636
V. Le Houérou- 0000-0001-7189-242X

Recently, plant surfaces have attracted great attention given their fascinating functionalities, particularly unique adhesive properties, which are largely resulting from their diverse surface structuring. This paper contributes to the advanced adhesion mechanics investigation on complex biological surface morphologies. Elastomeric replica of three different plant leaves, comprising morphologies at a broad scale (0.5-100 μm), with distinct shapes and complexity, and of a smooth surface were studied in contact with an adhesive probe. To perform precise adhesion measurements, an ultra-nanoindenter was modified based on the JKR (Johnson-Kendall-Roberts) mechanics and equipped with an in-situ real-contact visualization system. The adhesion force on all surfaces was systematically investigated regarding the pre-load conditions. The results were analysed in the light of Hertzian and JKR theories, and underlying morphology-specific mechanisms were identified. A close examination of contact image-force data synchronization revealed unique attachment-detachment mechanisms, arising from different pre-loads and topographies. A significant influence of pre-load on adhesion was observed on the surface with fine micro-structuring and complex morphology, no specific influence was recorded for the remaining two. An overall comparison demonstrates a significant reduction in adhesion on coarse cone-shape patterns and complex micro-structures. The specific adhesion mechanisms arising from biological morphologies may offer assistance to design bio-inspired smart interfaces.

Keywords: Adhesion mechanics, JKR theory, PDMS replica, *in-situ* imaging, bioinspired micro-structures

1 Introduction

Adhesive phenomena are found in a plethora of biological systems as well as in numerous man-made engineering applications, especially when the surface to volume ratio gets extremely increased.[1–5] Undoubtedly, the adhesive characteristics of interacting surfaces are a key feature to control system's performance and durability.[4,6] Consequently, it appears of paramount importance to precisely tune adhesive properties, especially in recently emerging micro- or nano-contact applications.[2,7,8] A well-recognised way to adjust the adhesion characteristics relies on modifying the surface chemistry.[9–12] Another approach consists in introducing surface texturing on the interacting surfaces.[13–17] The pioneering work by Fuller and Tabor back in 1975, proposed a reduction in adhesion force by incorporating surface roughness.[18] In the last four decades, various approaches have been published utilising notably defined geometrical asperities (square, cylindrical or hexagonal pillars, spherical dimples, etc.) to study the influence of surface morphology on adhesive response.[13,15–17,19–24] Few others explored adhesion characteristics and contact formation mechanisms on surfaces decorated with ripple or wrinkle shaped texturing.[7,25–29] Regardless of all these studies, the adhesion mechanisms are not completely understood yet, since the type and complexity of morphologies can cause unique and distinct adhesion behaviours.[7,13,17,30–39]

In nature, adhesion also plays an important role, e.g. for the interaction of animals with plant surfaces or with the inanimate environment.[1,40–43] Broadly mentioning, insect attachment pads evolved in a manner to assist in sticking to or climbing on various plant surfaces,[41,44–47] while on the counterpart, most of the plant leaves possess surfaces obstructing or reducing insect attachment.[48–51] Leaf surfaces are often decorated with species-specific surface structuring of different size, ranging from few nanometres to few hundreds of micrometres, having distinct shape and complexity, both at various levels of hierarchy.[52–56] This induces some optimised surface functionalities such as surface wettability, anti-adhesive properties, friction reduction, antifouling, slipperiness against insect attachment and optical properties, just to name a few.[44,50,52,53,57–62] As a result, these surfaces gained a lot of attention from the contact mechanics community which intended to investigate, get inspired, and thus transfer innovative insights into biomimetic surface applications.[14,59,63–70] However, the relationship between structures and functions is not straight forward, keeping in mind that these plant surface phenomena are driven by a complex interplay of material composition, heterogeneous surface chemistry and diverse surface structuring leading to a highly sophisticated system to investigate.[53,61,62] A possible simplification, that has been used in the past, consists in the

precise replication of the complex structural morphologies of plant surfaces onto polymeric surfaces.[49] This facilitates a methodical investigation of the role of surface morphology, without the influence of physico-chemistry aspects.[49,71,72] Although the advancement in the micro-structured surface fabrication technologies in the past decades made possible to generate a vast kind of micro- or nano-structures,[19,73–79] it is still far to realise the diversity and intricacy of biological surface structures.[52–54,56] Nevertheless, several papers have been published offering different methodological approaches to replicate the surface structures directly from original plant leaves onto the various polymeric substrates.[80–85]

Over the recent years, there has been a growing interest towards the *in-situ* contact visualization when conducting adhesion investigations, and it became possible with the latest innovations in the field of optical imaging.[7,19,21,22,25,86–89] Surely, *in-situ* imaging offers a detailed insight into the contact junctions over the apparent contact area, as well as attachment/detachment mechanisms. However, much of the research performing *in-situ* contact visualization has been limited to either smooth surfaces[87,90–92] or regular micro-structured surfaces.[7,16,19,21,23,25,31,89] Indeed, most of the contact mechanics investigations based on plant leaf surfaces could not achieve real-time visualization of the contact formation, down to cellular or sub-micron-sized cuticular fold level.[49,71]

Taken all together, in this work, we use the adhesion mechanics approach to methodically investigate the contact formation (closely inspired from insect-plant interactions) between biological structured replicas and a model adhesive tip. Three model plant leaves were selected and replicated onto polymeric samples, considering a broad morphological range in terms of their structure's size, shape and hierarchy. By considering the advantageous aspects and final positive replica characteristics relevant to our research specifications, we employed the replication technique presented by Kumar *et al.* 2018, which uses epoxy resin for generating negative moulds and producing the final replica on Polydimethylsiloxane (PDMS) substrates.[80] The force range that corresponds to plant-insect interactions falls in the few mN range, and therefore calls for a precise experimental setup.[45,93,94] Such a low force range and high sensitivity can be accomplished with a nano-indenter like apparatus.[95–97] Thus, we introduce an adhesion force tester (modified nano-indenter) to perform low-range adhesion force measurements under precise load or displacement control. Furthermore, the modified apparatus permits to visualise the *in-situ* contact on the complex micro-structured surfaces. At first, this paper quantitatively investigates adhesion force characteristics on the PDMS leaf replicas and on a smooth PDMS surface benchmark, and critically examines the influence of

pre-load and surface morphology. Furthermore, the dedicated *in-situ* imaging offers a comprehensive insight into the real and apparent contact areas, along with the understanding of attachment and detachment mechanisms.

2 Results and Discussion

2.1 Surface Morphologies

The results of SEM surface morphological investigation, shown in **Figure 1**, prove the high precision of PDMS replicas, made directly from original plant leaves by using Epoxy–PDMS replication. All three plant leaf surfaces, *H. brasiliensis* leaf with wrinkle-shaped fine microstructures (Figure 1.a and Figure 1.b); *L. discolor* surface with cone-shaped coarse micro-structures (Figure 1.d and Figure 1.e); and *L. chinensis* with complex hierarchical microstructures (Figure 1.g and Figure 1.h) were replicated to PDMS with high fidelity. After the n-heptane treatment, all samples were perfectly restored back by de-swelling to their original state without damage, as proven in Figure 1.c, 1.f and 1.i.

2.2 Adhesion Force Characteristics

Adhesion force measurements were carried out for each polymeric replica as well as for a smooth PDMS surface. Data sets were recorded by carrying out in total 5 to 7 experiments spotted on the samples for each surface type. **Figure 2** shows a plot obtained from a typical pull-off adhesion force measurement on a smooth PDMS sample. Adopting the standard contact mechanics formalism, the absolute maximum negative force value during the retraction phase corresponds to the adhesion pull-off force (F_{ad}), as reported in Figure 2.[7,98] In order to investigate the effect of pre-load (F_L), adhesion experiments were performed at the same spot, for seven different F_L values: 0.5, 1.0, 1.5, 2.0, 2.5, 3.0 and 3.5 mN, keeping all other test parameters (loading/unloading rate, retraction speed, and test duration) and conditions constant. In the following sub-sections, the results on attachment and detachment mechanisms, alongside with the results from the pre-load effects on adhesion force characteristics, are presented and discussed consecutively for each surface type. For reading convenience, hereafter, only genus name is used to address each PDMS replica sample instead of full species name: *Hevea* replica for *H. brasiliensis*, *Ludisia* replica for *L. discolor,* and *Litchi* replica for *L. chinensis*.

2.2.1 Smooth PDMS

A force-displacement-time curve of an adhesion measurement, for a whole test cycle, on smooth PDMS sample at a pre-load (F_L) of 1.5 mN is shown in Figure 2.A. The measured adhesion force (F_{ad}) is 0.827 mN. Still image sequences from the *in-situ* contact video (see the Video 1 in supporting data) of the adhesion test at the various points of interest (a-f) are set out in Figure 2.B. With regard to the kinetics of a smooth PDMS contact, attachment and detachment events appeared very continuous, homogenous and circular in shape over the whole contact cycle. The real contact area increased with increasing normal load and started decreasing once the retraction part began, involving the well-known adhesion hysteresis.[99] The point (a) in the graph indicates the contact point at zero load, right after the snap-in contact has taken place (not shown in the graph) ending the approach step. Therefore a small contact could be seen in the corresponding *in-situ* contact image (Figure 2.a). At this state, tip and substrate already formed a solid-solid intimate contact. After this, the continuous loading phase began and the tip slowly is pressed onto the substrate surface under a precise load controlled loading, at a rate of 83.3 μN/sec. Point (b) in the graph represents the phase when the system can relax under the constant maximum load: a closer observation of point b (radius ≃ 184 μm) and point c (radius ≃ 188 μm) exhibited a small increase in radius at point c, which witnesses this material relaxation.

The JKR theory is suitable to describe the contact mechanics for soft compliant materials with high adhesion energy.[100,101] In order to confirm the applicability of the JKR theory, one could utilize the dimensionless physical parameter, Tabor's parameter (μ_T), which is defined by:

$$\mu_T = \left(\frac{RW^2}{E^{*2}Z_0^3}\right)^{1/3} \quad (1)$$

Here, R is the relative radius of curvature of the contacting bodies, and can be estimated with $1/R = 1/R_1 + 1/R_2$ (with R_1 and R_2 being the radii of the contacting bodies), E^* is the effective elastic modulus, which can be calculated using $E^* = E/2(1-\nu^2)$; E is the PDMS Young's modulus and ν is the Poisson's ratio ($\nu_{PDMS} = 0.5$).[90] The E value for PDMS was calculated as 1.01 ± 0.01 MPa by using the classical JKR model fitting on smooth PDMS substrate. [102,103] Z_0 is the equilibrium separation of the surfaces in the Lennard-Jones potential and usually comes in between 0.3 and 0.5 nm.[90] If μ_T value is greater than 5, then a contact can be well described using the JKR theory.[101] By utilising the known values from the given

experiment's formation: $R_1 = 1.5$ mm (tip), $R_2 = \infty$ (flat surface), μ_T value would result in the range of ≈ 3500- 5800. This value range clearly suggests the well applicability of JKR model in this experiment. Further investigation of the retraction part of the curve shows, that the measured value of the contact diameter ($2a_d$) at the absolute zero load condition (Figure 2.d) was found to be 348 µm. The contact diameter ($2a_e$) at the very lowest force point, *the point of detachment instability*, where the contact diameter abruptly vanished to zero, was measured to be 219 µm (Figure 2.e). This finding is in good accordance with the previously established JKR theory, which predicts the following relation $a_e = 0.63a_d$.[104,105]

Effect of pre-loading: The results reported in **Figure 3** show the effect of F_L on F_{ad}. Here, F_{ad} values appear to be independent ($F_{ad} \simeq 0.809$ mN) from F_L variations, which is again in good agreement with the Johnson, Kendall, and Roberts (JKR, 1971) model,[102] as reported in previous studies.[106,107] The relaxation time for PDMS is reported to be in the order of 0.05-0.5 s, significantly less as compare to the contact time applied in this investigation.[108] Hence, it could be assumed that this contact system behaves more likely as elastic since loading and unloading phases could be considered as quasi-static.[108] Actually, all the tests in this investigation were performed slowly enough to minimize the viscous effects of material. Moreover, no effect of loading history on the adhesion force values in the investigated force range was noticed, as supported with the results stating the independence of F_{ad} from F_L. Hence, this observation very much supports that our test protocol is adequately complying with the standard JKR adhesive model. Therefore, these considerations on smooth PDMS contacts validate our test protocol, notably concerning the loading/unloading speeds and relaxation time which ensure a quasi-static test.

2.2.2 Hevea Replica

An *in-situ* video of the adhesion test for an entire contact cycle on *Hevea* replica at a F_L of 1.5 mN is shown in Video 2 (supporting data). To gain a better understanding of the attachment dynamics, we closely analysed the zoomed-in *in-situ* image captures. The fine structured surface of *Hevea* replica is easily recognizable (**Figure 4**) and it is clearly possible to distinguish between the true contact area (in bright contrast) and the area out of contact (in dark contrast). The contact formation initiated at the second level of micro-structuring (fine cuticular folds), and as the contact border advanced a whole cell was pulled in an intimate contact.[19] At the maximum load, even though each cell appeared to be in full contact, the cell boundaries (outer line surrounding a cell, first level of structuring) were left out of contact (darker line areas). Afterwards, as the detachment event began, two distinct contributions in contact separation

mechanisms could be identified when one closely observes the detachment sequences: (i) cell boundaries initiated and assisted the interfacial crack propagation during the detachment sequence and (ii) each cell, as a whole detached at a time, behaving as an individual contact point of instability. The interfacial crack initiation began at the cell boundaries around the outer periphery of the whole contact region and then the crack further spreads toward inner areas. A similar kind of detachment phenomenon has been reported by Jin *et al.*,[7] where adhesive contact was formed between a rigid sphere and a rippled elastic surface.

Different contrast during attachment and detachment phases: Another interesting finding from a closer observation on the zoomed-in *in-situ* videos is the distinct colour contrast at the contact periphery for the attachment and detachment cycles (Figure 4). Continuous *flowing-type* of the contact advancement mechanism could be observed during attachment, as illustrated in Figure 4.a and Figure 4.b, while a sharp contrast on contact edges is exhibited during the detachment (Figure 4.c and Figure 4.d). We believe, that the higher edge sharpness in the detachment sequence could be attributed to an increase in local strain and thus led to adhesion profiles on edges showing perpendicular connection fillet. Such a phenomenon has also been mentioned in a previous study by Charrault *et al.*[90].

Effect of pre-load: **Figure 5** shows adhesion force characteristics with increasing normal pre-load, for *Hevea* replicas. We investigated further the *in-situ* contact images to compute the normalized contact area (A_n) at the full loading condition, for all the F_L values (Figure 5, blue data points). A clear increase in F_{ad} from 0.384 mN to 0.490 mN was observed with increasing F_L from 0.5 to 2.5 mN. However, adhesion force might get saturated with a further increase in F_L above 2.5 mN.[14,22] The increase in F_{ad} could be explained with the filling-up of fine microstructure pockets between the wrinkles (cuticular folds), while increasing F_L. A similar phenomenon has been found also in previous studies.[14,15,24,109] Actually, at a low F_L (0.5 mN) value, only partial contact occurs at the very top of cuticular folds, resulting in a small normalised real contact area, $A_n = 0.44$, reported in Figure 5. With further increasing F_L, the tip material progressively fills up the small non-contact gaps between the wrinkles, hence resulting in an increase in adhesion force by a factor of about 30 %. One can also notice in Figure 5.I and Figure 5.II that there was an evidently larger true area still left in contact even when load was removed (at the absolute zero load), for the higher pre-load ($F_L = 3.5$ mN) condition in comparison to the smaller pre-load $F_L = 0.5$ mN. This supports the previous statement and confirms that the observed increase of F_{ad} for *Hevea* replica is caused by its specific fine micro-structuring.

Interestingly, A_n increases in the beginning with increasing F_L until 2.5 mN is reached. Above this value, A_n appears to get saturated at higher pre-loads (3.0 mN and 3.5 mN).
A_n curve shows a similar dependency to F_L as the adhesion force (Figure 5) does. This similar trend corroborates the filling of microstructures at high pre-loads, which leads to saturate at high F_L values: A_n tends to saturate at 0.6, and could never reached 1 (the latter meaning complete full contact). The spherical shape of the tip contributes to this experimental fact since it causes a parabolic (non-flat) pressure distribution.[98,110] This also further implies that the full intimate contact arose in the middle region, partial contact slowly spreading at the outer edges with increasing F_L.[13,19]

2.2.3 Ludisia Replica

As illustrated in **Figure 6**.a, the real contact (the bright circular areas) always occurred at the very top of the conical shaped micro-structures of the *Ludisia* replica, for the complete pre-load range (0.5-3.5 mN). Interestingly, one may note that, the real contact area was significantly lower than the apparent area, and thus is reducing A_n to 6.91% (at the full loading condition for F_L = 1.5 mN), owing to the specific conical shaped topography. A closer examination of *in-situ* video (see supporting Video 3 in supporting data) for a whole test run revealed that the contact formation was continuous, and real and apparent contact grew locally and homogenously circular in shape. The microstructures in middle region contributed more in bearing the contact pressure, as confirmed by the larger size bright spots distributed in the middle area if compared to the outer side (Figure 6.b – threshold image). This can be attributed to the *Hertzian*-type parabolic pressure distribution given for two contacting bodies.[98,111] This holds likewise for the whole F_L range investigated. As soon as the detachment step is initiated, each true contact periphery instantly started separating, without exhibiting any explicit contact hysteresis.

Further on, a local examination of the contact formation on *Ludisia* replica pointed out that, the attachment-detachment mechanism on an individual microstructure could be considered similar as to the contact of single asperities on a smooth surface. Indeed, it is meaningful to approximate this behaviour as an inverted case of a half-sphere pressed on a flat surface contact model: at a small scale, the top of each cell tip of *Ludisia* replica behaves like a spherical asperity, that is locally forming contact against the almost flat surface of the probe. By analysing the surface topographies, average real contact densities and contact formation for a given pre-load, one can assume that the coupling of elastic displacements between a cell microstructure and its neighbouring cells is negligible.[21,112] Thus, we used an approach previously introduced by

Romero *et al*. 2014 and Yashima *et al.* 2015, to validate the *Hertzian* character of the contact at the local cell structures scale for *Ludisia* replica.[21,89]

A standard contact under *Hertzian* conditions for a sphere in contact with a half-space flat surface[102] can be computed using equation 2.

$$P_c = E^* \sum \frac{4\, a_i^3}{3\, R_i} \tag{2}$$

With E^* is the effective elastic modulus, which can be here calculated using $E^* = E/2(1-\nu^2)$; E is the PDMS Young's modulus and ν is the Poisson's ratio (ν_{PDMS} = 0.5).[87,90] The E value for PDMS was calculated as 1.01 ± 0.01 MPa by using the classical JKR model fitting on smooth PDMS substrate;[102,103] R_i is the normalized radius of curvature of the circular cell tip of the *Ludisia* replica; a_i represents the radius of the local real contact forming at each individual tip (Figure 6.a), and was computed by locating real contact spots on the threshold image, as illustrated in Figure 6.b. F is the externally applied normal load, whereas P_c is the summation of inversely computed local (at real contact junctions) normal loads, assuming the *Hertzian* contact model obeyed locally. Using the equation 3, P_c was calculated at different loads F, for loading and unloading cycles. The P_c versus F results are plotted in **Figure 7**, and apparently loading and unloading data points found to be closely following a linear behaviour, with R-square values of 0.998 and 0.997, respectively.

Moreover, P_c values for the unloading cycle trace back to nearly zero, and overlap quite well with the loading curve, thus validating the assumption of the *Hertzian* local contact model for the *Ludisia* replica. Accordingly, our results are supporting the assumption of a negligible elastic couplings in between the neighbouring cells so that at this scale each asperity in contact can be considered as an individual non-adhesive contact.

Effect of pre-load: Here, the F_{ad} values found were the lowest compared to all other surfaces investigated. For instance, at the pre-load condition of 1.5 mN, F_{ad} (0.014 mN) was reduced by about 98% in comparison to a smooth PDMS surface (0.809 mN). This reduction in F_{ad} holds for all F_L conditions. F_{ad} results as a function of F_L are presented in **Figure 8** and clearly illustrate no notable variation in F_{ad} with increasing F_L. This is consistent with the validation of the local *Hertzian* contact on each cell of the *Ludisia* replica surface and thus supports our assumption of non-adhesive contact at local scale. Our results also suggest that loading and

unloading at small scale can still be considered as quasi-static since no viscous hysteresis was detected.

2.2.4 Litchi Replica

An *in-situ* video for a whole adhesion test cycle, on *Litchi* replica, at a F_L of 1.5 mN is presented in Video 4 (supporting data). At first sight, contact mechanics appeared to be very complex, given the fact of the high complexity of surface microstructures of *Litchi* replica combined with the obvious video quality limitations. Indeed, one could point out that the *in-situ* videos on *Litchi* replica lacked in-detail clarity in comparison to other three surfaces studied, pointing out the technical limitations of proposed technique for certain highly complex morphologies. Nevertheless, it was visible that the real contacts (bright spots) were discretely distributed over the apparent contact zone, related to the heterogeneous and random surface structuring. To gain a better understanding of the attachment mechanism, zoomed-in videos have been checked and the local contact zones were analysed. As soon as the loading event started, fine cuticular folds began to form partial top-contact. With further increase in pre-load, the overhanging fine structures (cuticular folds) of an individual '*rose-flower-shaped*' unit accumulated together and started forming a localised cluster of units, as could be seen as close bright spots appearing in the *in-situ* video, at the fully loaded condition (dashed domain in **Figure 9**.II). After the full loading phase, during the retraction cycle a particular feature was observed: the sudden fluctuating behaviour and profile of the force-displacement curve, as presented in Figure 9.I (like the point "C" for instance), which called for further analysis. We examined the *in-situ* video sequence corresponding to the position of major sudden fluctuations on the force-displacement curve. This became possible thanks to the real-time image-data point synchronization. A series of *in-situ* contact images corresponding to various points of interest during the retraction part of the force-displacement curve are illustrated in Figure 9.II. This fluctuation behaviour could be understood by taking into account two energy factors: (1) the bending of overhanging patterns leading to localized storage of the elastic strain energy, and (2) the agglomeration of '*rose-flower-shaped*' unit (micro-morphologies) gathered in a short range coupling style. During the unloading phase, the bended folds started popping out, and thus caused a sudden release of the stored elastic energy that acted against the adhesion force.[36]

These real contact morphologies are discretely distributed over the apparent contact zone, thus implying the individual agglomerated cluster released the stored energy locally with the instable separation. This behaviour appeared to be more force sensitive, and therefore, it was more pronounced and clearly visible at higher pre-load (F_L = 3.0 mN as compared to 0.5 mN), which

can be seen in Figure 9.II. This might be attributed to similar force-dependence mechanism as found in *Hevea* replica (section 2.2.2).

Effect of pre-load: **Figure 10** shows the results from the effect of F_L on F_{ad} characteristics for *Litchi* replicas. An initial increase in F_{ad} with raising F_L, until 3.5 mN is clearly visible. Since the previously described parameter range (i.e. F_L between 0.5-3.5 mN) did not provide a particular transition, we therefore continued the tests up to F_L = 5.0 mN. Thus, F_{ad} appeared to get saturated with a minor variation from 4.0 mN onwards. This could be explained with the force sensitive phenomenon associated with the complex surface morphology of *Litchi* replicas previously discussed. At low F_L values, true contact formed partially only on the very top of overhanging micro-structures, whereas with increasing in F_L more real contact is formed leading to higher adhesion measured at the detachment. Actually, one could note in the Figure 9.a and Figure 9.A, that there was a larger true contact area for higher F_L (3.0 mN) as compared to low F_L (0.5 mN), at the absolute zero load condition during the unloading cycling.

3 Overall Comparison and Conclusions

In the present paper, a systematic study of adhesion contact mechanics at a low force range on high-precision transparent replicas of biological micro-structured surfaces is presented. In order to achieve such detailed investigation, we successfully developed an innovative technique for *in-situ* contact visualization, allowing the analysis of attachment-detachment mechanism on transparent replicas of complex biological surface morphologies. In this study we experimentally evaluated the pull-off adhesion force of four distinct surfaces and analysed its dependence to pre-load and surface morphology. Based on the key findings of this investigation the following conclusions can be drawn:

- A significant difference in F_{ad} between the all four surfaces was found, as presented in **Figure 11**, for F_L = 1.5 mN condition. The same trends appear for all other F_L conditions tested as well.
- Apparently, the smooth PDMS surface exhibited the highest value of adhesion force ($F_{ad} \simeq$ 0.809 mN, at F_L = 1.5mN) out of all the four tested surfaces (Figure 11). On the surface with fine wrinkle shaped micro-structuring (*Hevea* replica) F_{ad} is reduced by 42.5 % ($F_{ad} \simeq$ 0.465 mN at F_L = 1.5 mN) in comparison to the smooth PDMS surface. However, the adhesion force of the *Hevea* replica is still significantly higher in comparison to the other studied micro-structured surfaces. The surface showing coarse sized micro-structures (*Ludisia* replica) and the surface with complex hierarchical structuring (*Litchi* replica) both showed

a markedly lower value of adhesion force, with F_{ad} = 0.014 mN and 0.035 mN respectively. The large reduction in adhesion force in the case of *Ludisia* replica could be attributed to the specific structure shape which favours local adhesion-free (*Hertzian*-like) contacts. This differs to what has been demonstrated in some previous studies of adhesion enhancement by using soft and compliant geometries with high aspect ratio.[32,35,66,113–115] Moreover, it is interesting to note in the Figure 11 that the adhesion force plot clearly follows a similar decreasing trends as the A_n plot. This could be interpreted as a confirmation of the correlation between the adhesion ability and the contact surface splitting, although we believe that local phenomena inducing large strain rate during detachment may overcome this rule. Unexpectedly, further analysis consisting of the normalization of F_{ad} by A_r did not permit to get additional insights in this respect.

- Contrary to smooth PDMS and *Ludisia*, the surface of *Litchi* and *Hevea* replicas demonstrated an increase in F_{ad} with F_L, which was attributed to the filling of fine microstructure pockets at high pre-loads.
- Thanks to the newly developed method of *in-situ* visualization, the distribution of real contact zones reveals a high dependency on size and morphologies of the surface structures and also exhibits distinct attachment and detachment phenomena.

The new *in-situ* contact visualisation method, its technical advancement and the results based thereon being presented in this study open up a promising direction in the understanding of contact formation on high-precision replicas of complex biological surface structures. The insights gained from this study, especially concerning force-dependent adhesion behaviours associated to morphology dependent attach-detach modes, may provide a valuable basis for designing novel bio-inspired functional surfaces with (fine-)tunable adhesion properties at a local scale. As prospects, the individual contribution of each level of hierarchical surface structuring on the adhesion force characteristics appears of prior importance.

4 Experimental Section

4.1 Investigated Biological Surfaces

Three different plant leaf surfaces were selected for this study, on the basis of different size, distinct morphology and complexity of their surface structuring. Rubber tree (*Hevea brasiliensis*; adaxial, i.e. upper leaf surface) shows two levels of structuring consisting of "puzzle piece-shaped" epidermal cells covered by fine cuticular fold microstructures (cf. Figure 1.a), with both height and width of about 0.5-1 µm and an intermediate spacing of 0.5-1.5

µm.[49] Jewel orchid (*Ludisia discolor*; adaxial) exhibits circular cone-like shaped microstructures (cf. Figure 1.d) with a diameter of about 50-100 µm and a height of about 50 µm.[80] Lychee (*Litchi chinensis*; abaxial, i.e. lower leaf surface) has a complex hierarchical surface structuring (cf. Figure 1.g) consisting of 'rose-flower-shaped' units inducing undercuts and overhanging substructures.[49] Additionally, previous work by *Prüm et al.*[50] showed that the leaf surfaces of *H. brasiliensis* and *L. chinensis* possess anti-adhesive properties for insects resulting from their specific micro structuring. For better morphological visualization, three-dimensional scan animations for all three leaf surfaces are presented in supporting data (Video 7, Video 8 and Video 9). All leaves used in this investigation were freshly collected just before processing the replication. Corresponding plants were grown in the Botanic Garden of the University of Freiburg, Germany.

4.2 Preparation of PDMS Replicas and Smooth Surfaces

PDMS (Polydimethylsiloxane), a silicone based soft elastomer, offers various key advantages: easy handling, low cost, non-toxicity, low surface energy ($\gamma = 22$ mJ.m^{-2}) and low elastic modulus ($E = 0.5$-4 MPa).[116] Because of its high γ/E ratio, it is suitable for adhesion mechanics studies and has been widely used in the past by various researchers.[21–23,87,90,106] This silicon-based elastomer has a very low glass transition temperature (-120 °C). It gets easily cross-linked into a very stable elastic network, showing high chemical stability at room temperature, and no explicit interaction with other material.[117] Importantly, PDMS exhibits high optical transparency, thus being a perfect applicant for achieving the *in-situ* contact visualization.[118]

Surface microstructures from the original plant leaves were precisely transferred onto PDMS, using the two-step replication technique described elsewhere.[80] A simplified description of the replication process is schematically presented in Figure S1 (supporting data). At first, negative moulds were developed with two components epoxy resin (Epoxydharz HT 2, R&G Faserverbundwerkstoffe GmbH, Germany) directly from the original fresh plant leaves. Fresh plant leaves were cut into small pieces (approximately 4 cm × 4 cm), and immediately secured onto a plastic petri dish with a double-sided adhesive tape. Subsequently, the uniformly mixed bubble free epoxy mixture (resin to hardener ratio of 10: 4.8) was steadily poured onto the leaf sample surfaces. After curing for 15 h at ambient conditions (temperature = 20-25°C and relative humidity = 40-60%), plant leaves were separated from negative epoxy moulds. In the case of *L. chinensis* leaves, the demoulding was fulfilled by a special anti-stiction step comprising the treatment of negative replica sample in an aqueous solution (60 g/100 ml) of potassium hydroxide (KOH, ≥85%, p.a., Carl Roth GmbH & Co. KG, Karlsruhe, Germany) at

60 ± 3°C for 20 h. In step two, negative epoxy moulds were filled up with low-viscosity Polydimethylsiloxane (Bluesil ESA 7250 A & B kit, Bluestar Silicones GmbH, Germany) mixture (monomer to cross-linker ratio of 10: 1) and were kept in a vacuum chamber for one hour to remove air entrapped at the interface. After curing at 75°C for 3 h, cross-linked PDMS replicas were peeled off from the negative moulds. Each replica sample was quality inspected for any replication imperfection, using an optical stereo microscope. Four samples were developed for each investigated surface type, to ensure statistical representativeness during adhesion tests. Smooth PDMS samples were produced by curing the same PDMS mixture in a freshly opened flat bottom glass petri dish.

All samples (PDMS leaf replicas as well as the smooth PDMS samples) were swollen in a solution of n-heptane and 1-dodecanethiol (0.01 %) for overnight to remove the sol fraction (to extract the remaining unreacted free chains). After then, all the swollen samples were dried at ambient room conditions for at-least 24 h to restore back to their original state.[99,119,120]

4.3 Surface Characterization

Surface morphology visualization and characterization was done using scanning electron microscopy (Leo 435 vp, Leica, Wiesbaden, Germany and Hitachi SU8010, UHR FE-SEM, France). For the plant leaf samples, fresh leaves were dehydrated in methanol solution and dried by using critical point drier (LPD 030, Bal-Tec).[121,122] In order to avoid surface charging, all samples (plant leaves, PDMS replicas, and replicas after n-heptane solution treatment) were metalized with a thin (ca. 10 nm) coating of gold (Cressington Sputter Coater, 108 auto) after being mounted on aluminium stubs (Plano GmbH, Wetzlar, Germany) and side walls coated with conductive silver paint (Acheson Silver DAG 1415M, Plano GmbH, Wetzlar, Germany). All SEM examinations were performed in the 30°- 45° tilting angle range. In addition, three-dimensional morphological scan of all fresh plant leaf surfaces was visualized and recorded with a confocal laser scanning microscope (LEXT OLS4000, Olympus Corporation, Japan).

4.4 Adhesion Testing

4.4.1 Description of the Modified Adhesion Force Tester

In 1971, Johnson, Kendall and Roberts (JKR) proposed a theory to describe the contact area of two elastic bodies in contact while considering adhesive forces acting between them.[102] The key characteristics of this theory include a finite non-zero contact at the zero normal load condition and a minimum negative (tensile) force (F_{ad}) required to separate the contacting bodies during the detachment cycle. In this work, the adhesion investigation was performed

with a JKR contact mechanics based apparatus, and described in-details in the following section. An ultra-nanoindentation tester (UNHT³, Anton Paar Tritec, Switzerland) with a high-resolution load-control of 3 nN and a depth resolution down to 0.3 nm was modified to perform low range adhesion force measurements, together with *in-situ* contact visualisation, as illustrated in a simplified schematic in **Figure 12**. Indeed, a dedicated optical system was introduced into the equipment, permitting high-resolution differential contrast microscopy based on transmission light microscope principle: a light beam shines from the probe and propagates through the tested substrate.[123,124]

In our investigations, since the size of the probe (half sphere of 1.5 mm radius) and the substrate patterning are small, it was delicate to incorporate the optical prerequisites associated to transmission light microscopy within the adhesion tester. White light from a fibre optic cold light illumination (KL 1600 LED, Schott AG, Germany) shines at the tip, via passing from a polarizer filter, and focused with a condenser lens onto the tip opening spot, with the purpose to get high-intensity illumination (Figure 12). A special tip (**Figure 13**) was fabricated with an internal micro-hole (radius = 0.5 mm) and with a micro-metal machining finished (alighted at an angle of ca. 45°) on top of the tip, so that the light beam is perpendicularly reflected and follows a path in the direction to the soft probe. An analyser along with an objective lens and a high definition colour camera (Basler acA3800-14uc, with a 10Mpix CMOS sensor, Germany) lie just under the substrate surface. This optical setup is mounted on a micromanipulator, benefiting to precisely focus on contact spot. The transmitted light beams through the contact junctions, where both surfaces (PDMS-PDMS) are in real-contact with matching refractive index, leading to high contrast bright spots. Light get randomly scattered over the area where no intimate contacts (PDMS-air interface) were established and thus appears as dark domains. Polarizer and analyser filters facilitated to obtain sharp yielded contact edges. Furthermore, the apparatus is equipped with a custom-build dedicated electronic system that enables simultaneous recording of the video frame in real-time synchronization with the corresponding force data points.

4.4.2 Model Adhesive Tip

A particular caution was paid to the soft elastomeric adhesive tip which was fabricated using a two-step moulding process. In the first step, a thick Polymethyl methacrylate (PMMA) substrate was locally heated up till ca. 100 ± 5°C, with an air heating gun. A sapphire ball (Edmund Optics, United States) with a radius of 1.5 mm and surface roughness of Ra = 0.005 µm was gradually pressed down until the ball half subsided into the PMMA surface. After cooling for 30 min, the ball was separated out from the bulk with a vacuum suction gripper, and

consequently provides a negative impression on the PMMA surface. This latter was then filled up with a PDMS mixture (prepared with same mixing protocol as described in section 4.2) and degassed in a vacuum desiccator for 20 min to remove any air bubble that could be trapped during pouring. The homebuilt tip holder evoked previously (Figure 13) consists of the assembly of an external screw thread and a nut attachment at its very end. Tip assembly was gradually put on top of the PDMS mixture which filled PMMA mould (Figure 13.b). During the PDMS curing process, the PDMS mixture filled up by capillarity the small gaps formed at the thread in between stud and bolt, as illustrated in Figure 13.a, thus ensuring a good anchorage of the PDMS tip with the holder.

Additionally, we observed that the PDMS level also raised up inside the drilled hole, consequently promoting a strong bulk attachment of PDMS tip with the tip holder (Figure S2 in supporting data). Tip's centre alignment with the centre of the PMMA mould was essential to get a uniform contrast all over the whole contact image during the *in-situ* visualization: the development of a perfectly aligned tip required several attempts (typically up to 4-5 tips) to become successful. After development, each tip assembly was checked under optical microscope and non-aligned tips were discarded. Furthermore, to examine any surface imperfection, tips were checked with a scanning electron microscope (Figure S2 in supporting data).

4.4.3 Surface Referencing

An important aspect during low force range tests is the accurate detection of the very-top point of contact i.e. surface referencing.[96] It becomes even more crucial, when both tip and substrate samples are made up of a soft matter polymer, where long-range adhesive forces in between tip and sample surface exist, and time-dependent creep of the polymer material during the referencing process itself could greatly influence the exactness of reference position and then further affect the accuracy of adhesion measurement.[97,125] In order to ensure a precise surface referencing, we used a separate parallel referencing tip-head made of metal against a metallic reference base, mounted with a high precision micrometre head, as shown in Figure 12. For the referencing process, at first both the reference tip and the adhesive tip are brought down together, in such a way so that the reference tip touched the reference base at first.

4.5 Experimental Protocol

All substrates were placed on rigid transparent glass plates and further fixed on the test platform. Prior to each set of tests, surface referencing was performed for each surface type. Then, the

adhesive tip slowly approaches near to the substrate surface. As the tip reaches in close proximity to the substrate surface, sudden snap-in (pull-in) takes place leading to a resulting pulling force. As the tip displacement increases, the normal load attains zero condition, corresponding to the initial zero load state in the force-displacement graph (Figure 2 - point a). At this state, the adhesion test can start and the adhesive tip begins forming contact under quasi-static loading, at a constant loading rate of 0.083 mN/s, until the defined normal pre-load (F_L) is reached. The adhesive tip is kept under constant F_L for a set time and then the tip is retracted under displacement control motion, at a constant speed of 0.83 µm/s. A graph of a typical adhesion test and pull-off force measurement (named F_{ad}) is shown in Figure 2. The range of F_L was kept low enough and substrate thickness was chosen large enough, so that the ratio of substrate thickness to mean contact radius was higher than ca. 10, thus the underlying substrate (glass slide) effect could be neglected.[90,103,126] All measurements were conducted in a climate controlled room (temperature = 22 ± 3°C, relative humidity = 50% ± 10%).

4.6 Image Processing

All the recorded *in-situ* videos were processed and analysed with the digital image processing tool *ImageJ* (v. 1.51p, National Institutes of Health, USA) permitting initial homogenous filtering, thresholding, and estimating the real contact and apparent areas.[127] The real contact area (A_r) was calculated by summing all the individual local real areas (A_{r_i}). For the apparent area (A_{ap}) estimation, multiple outmost peripheral point coordinates were sampled from all directions and fitted with a standard best-fit ellipse. The normalized contact area (A_n) is defined as:

$$A_n = \frac{\sum A_{r_i}}{A_{ap}} \tag{3}$$

5 Supporting Information

Supporting Information is available from the Wiley Online Library or from the author.

6 Acknowledgements

The authors would like to express their gratitude to the gardeners of Botanic Garden of the University of Freiburg for cultivating the plants used in this study. We are thankful to the electron microscopy platform and to the micro-nano-mechanic platform of Institut Charles Sadron, Strasbourg. We would also like to thank the German Research Foundation (Deutsche

Forschungsgemeinschaft: DFG), for funding support under the framework of International Research Training Group (IRTG) 'Soft Matter Science - 1642'.

7 Authors' contributions

C.K., V.L.H., and T.S. conceived the project idea. C.K. contributed towards the fabrication and characterization of replica samples. C.K. together with V.L.H and D.F designed the experimental technique. Adhesion experiments and data analysis were carried out by C.K. First draft of the manuscript was prepared by C.K., and critically corrected by V.L.H. and T.S. All authors have given approval to the final version of the manuscript.

8 Conflict of Interest

The authors declare no conflict of interest.

9 References

[1] M. Scherge, S. Gorb, *Biological Micro-and Nanotribology*, Springer Science & Business Media, **2001**.
[2] B. Bhushan, *Springer Handbook of Nanotechnology*, Springer Science & Business Media, **2010**.
[3] K. Kendall, *Molecular Adhesion and Its Applications: The Sticky Universe*, Springer Science & Business Media, **2007**.
[4] R. Kaneko, in *Proceedings. IEEE Micro Electro Mechanical Systems*, IEEE, **1991**, p. 108.
[5] N. Myshkin, M. Petrokovets, A. Kovalev, *Tribology International* **2005**, *38*, 910.
[6] A. C. Fischer-Cripps, *Introduction to Contact Mechanics*, Springer, **2000**.
[7] C. Jin, K. Khare, S. Vajpayee, S. Yang, A. Jagota, C.-Y. Hui, *Soft Matter* **2011**, *7*, 10728.
[8] N. R. Tas, C. Gui, M. Elwenspoek, in *Proceedings IEEE Thirteenth Annual International Conference on Micro Electro Mechanical Systems*, IEEE, **2000**, pp. 193–198.
[9] R. Maboudian, W. R. Ashurst, C. Carraro, *Sensors and Actuators* **2000**, *82*, 219.
[10] W. R. Ashurst, C. Carraro, R. Maboudian, *Device and Materials Reliability, IEEE Transactions on* **2003**, *3*, 173.
[11] E. Kroner, R. Maboudian, E. Arzt, *Advanced Engineering Materials* **2010**, *12*, 398.
[12] M. Dirany, L. Dies, F. Restagno, L. Léger, C. Poulard, G. Miquelard-Garnier, *Colloids and Surfaces A: Physicochemical and Engineering Aspects* **2015**, *468*, 174.
[13] E. Verneuil, B. Ladoux, A. Buguin, P. Silberzan, *The Journal of Adhesion* **2007**, *83*, 449.
[14] C. Greiner, A. del Campo, E. Arzt, *Langmuir* **2007**, *23*, 3495.
[15] D. Paretkar, M. Kamperman, D. Martina, J. Zhao, C. Creton, A. Lindner, A. Jagota, R. McMeeking, E. Arzt, *Journal of The Royal Society Interface* **2013**, *10*, 20130171.
[16] S. C. L. Fischer, E. Arzt, R. Hensel, *ACS Appl. Mater. Interfaces* **2017**, *9*, 1036.
[17] N. Cañas, M. Kamperman, B. Völker, E. Kroner, R. M. McMeeking, E. Arzt, *Acta Biomaterialia* **2012**, *8*, 282.
[18] K. Fuller, D. Tabor, *Proceedings of the Royal Society of London. A, Mathematical and Physical Sciences* **1975**, *345*, 327.

[19] V. Hisler, M. Palmieri, V. Le Houérou, C. Gauthier, M. Nardin, M.-F. Vallat, L. Vonna, *International Journal of Adhesion & Adhesives* **2013**, *45*, 144.
[20] J. Purtov, M. S. Elena V. Gorb, S. N. Gorb, *Applied Physics A* **2013**, *111*, 183.
[21] S. Yashima, V. Romero, E. Wandersman, C. Frétigny, M. Chaudhury, A. Chateauminois, A. Prevost, *Soft Matter* **2015**, *11*, 871.
[22] É. Degrandi-Contraires, A. Beaumont, F. Restagno, R. Weil, C. Poulard, L. Léger, *EPL* **2013**, *101*, 14001.
[23] L. Dies, F. Restagno, R. Weil, L. Léger, C. Poulard, *Eur. Phys. J. E* **2015**, *38*, 130.
[24] G. Castellanos, E. Arzt, M. Kamperman, *Langmuir* **2011**, *27*, 7752.
[25] C. S. Davis, D. Martina, C. Creton, A. Lindner, A. J. Crosby, *Langmuir* **2012**, *28*, 14899.
[26] Y. Rahmawan, C.-M. Chen, S. Yang, *Soft Matter* **2014**, *10*, 5028.
[27] C. S. Davis, A. J. Crosby, *Soft Matter* **2011**, *7*, 5373.
[28] D. Breid, A. J. Crosby, *Soft Matter* **2011**, *7*, 4490.
[29] D. Martina, C. Creton, P. Damman, M. Jeusette, A. Lindner, *Soft Matter* **2012**, *8*, 5350.
[30] G. Briggs, B. Briscoe, *Journal of Physics D: Applied Physics* **1977**, *10*, 2453.
[31] L. Heepe, A. E. Kovalev, S. N. Gorb, *Beilstein Journal of Nanotechnology* **2014**, *5*, 903.
[32] M. Lamblet, E. V. and Vilmin, A. Buguin, Silberzan, L. Léger, *Langmuir* **2007**, *23*, 6966.
[33] A. Peressadko, N. Hosoda, B. Persson, *Physical Review Letters* **2005**, *95*, 124301.
[34] A. Tiwari, L. Dorogin, A. Bennett, K. Schulze, W. Sawyer, M. Tahir, G. Heinrich, B. Persson, *Soft Matter* **2017**, *13*, 3602.
[35] N. J. Glassmaker, A. Jagota, C.-Y. Hui, W. L. Noderer, M. K. Chaudhury, *Proceedings of the National Academy of Sciences* **2007**, *104*, 10786.
[36] S. C. Fischer, K. Groß, O. Torrents Abad, M. M. Becker, E. Park, R. Hensel, E. Arzt, *Advanced Materials Interfaces* **2017**, *4*, 1700292.
[37] E. Kizilkan, S. N. Gorb, *Advanced Materials* **2017**, DOI 10.1002/adma.201704696.
[38] S. Vajpayee, K. Khare, S. Yang, C.-Y. Hui, A. Jagota, *Advanced Functional Materials* **2011**, *21*, 547.
[39] B. Persson, E. Tosatti, *The Journal of Chemical Physics* **2001**, *115*, 5597.
[40] E. Arzt, S. Gorb, R. Spolenak, *Proceedings of the National Academy of Sciences* **2003**, *100*, 10603.
[41] E. V. Gorb, S. N. Gorb, in *IUTAM Symposium on Scaling in Solid Mechanics* (Ed.: F. Borodich), Springer, **2009**, pp. 243–252.
[42] E. V. Gorb, J. Purtov, S. N. Gorb, *Scientific Reports* **2014**, *4*, DOI 10.1038/srep05154.
[43] J. Hazel, M. Stone, M. S. Grace, V. V. Tsukruk, *Journal of Biomechanics* **1999**, *32*, 477.
[44] S. N. Gorb, *Philosophical Transactions of the Royal Society of London A* **2008**, *366*, 1557.
[45] D. Labonte, W. Federle, *Philosophical Transactions of the Royal Society B: Biological Sciences* **2015**, *370*, 20140027.
[46] H. M. Whitney, W. Federle, *Current Opinion in Plant Biology* **2013**, *16*, 105.
[47] S. L. Young, M. Chyasnavichyus, M. Erko, F. G. Barth, P. Fratzl, I. Zlotnikov, Y. Politi, V. V. Tsukruk, *Acta Biomaterialia* **2014**, *10*, 4832.
[48] S. Poppinga, K. Koch, H. F. Bohn, W. Barthlott, *Functional Plant Biology* **2010**, *37*, 952.
[49] B. Prüm, H. F. Bohn, R. Seidel, S. Rubach, T. Speck, *Acta Biomaterialia* **2013**, *9*, 6360.
[50] B. Prüm, R. Seidel, H. F. Bohn, T. Speck, *Journal of the Royal Society Interface* **2012**, *9*, 127.
[51] L. Wang, Q. Zhou, *Scientific Reports* **2016**, *6*, 19907.
[52] W. Barthlott, M. Mail, B. Bhushan, K. Koch, *Nano-Micro Letters* **2017**, *9*, 23.
[53] K. Koch, B. Bhushan, W. Barthlott, *Soft Matter* **2008**, *4*, 1943.
[54] K. Koch, H. F. Bohn, W. Barthlott, *Langmuir* **2009**, *25*, 14116.
[55] C. Neinhuis, W. Barthlott, *Annals of Botany* **1997**, *79*, 667.
[56] W. Barthlott, N. Ehler, *Tropische und subtropische Pflanzenwelt* **1977**, *19*, 367.

[57] W. Barthlott, M. Mail, C. Neinhuis, *Philosophical Transactions of the Royal Society A* **2016**, *374*, 20160191.
[58] B. Bhushan, Y. C. Jung, *Progress in Materials Science* **2011**, *56*, 1.
[59] K. Koch, B. Bhushan, W. Barthlott, *Progress in Materials Science* **2009**, *54*, 137.
[60] W. Barthlott, C. Neinhuis, *Planta* **1997**, *202*, 1.
[61] H. Bargel, W. Barthlott, K. Koch, L. Schreiber, C. Neinhuis, in *The Evolution of Plant Physiology* (Eds.: A.R. Hemsley, I. Poole), Academic Press, London, **2004**, pp. 171–194.
[62] M. Eder, S. Amini, P. Fratzl, *Science* **2018**, *362*, 543.
[63] Y. Bar-Cohen, *Bioinspiration & Biomimetics* **2006**, *1*, 1.
[64] B. Bhushan, *Langmuir* **2012**, *28*, 1698.
[65] B. Bhushan, *Philosophical Transactions of the Royal Society A* **2009**, *367*, 1445.
[66] A. del Campo, C. Greiner, E. Arzt, *Langmuir* **2007**, *23*, 10235.
[67] S. Gorb, T. Speck, *Beilstein Journal of Nanotechnology* **2017**, *8*, 403.
[68] E. Kroner, J. Blau, E. Arzt, *Review of Scientific Instruments* **2012**, *83*, 016101.
[69] W. Barthlott, M. Mail, B. Bhushan, K. Koch, in *Springer Handbook of Nanotechnology*, Springer Nature Switzerland AG, **2017**, pp. 1265–1305.
[70] J. Busch, W. Barthlott, M. Brede, W. Terlau, M. Mail, *Philosophical Transactions of the Royal Society A* **2018**, *377*, 20180263.
[71] B. Prüm, R. Seidel, H. F. Bohn, T. Speck, *Beilstein Journal of Nanotechnology* **2012**, *3*, 57.
[72] C. Kumar, A. Palacios, V. A. Surapaneni, G. Bold, M. Thielen, E. Licht, T. E. Higham, T. Speck, V. Le Houérou, *Philosophical Transactions of the Royal Society A* **2018**, *377*, 20180265.
[73] M. Kim, K. Kim, N. Y. Lee, K. Kim, K. Shin, Y. S. Kim, *Chemical Communications* **2007**, 2237.
[74] G. Zhuang, J. P. Kutter, *Journal of Micromechanics and Microengineering* **2011**, *21*, 105020.
[75] X. Zhu, H. Chen, L. Zhu, H. Wang, W. Zhang, *Optical Engineering* **2014**, *53*, 117109.
[76] B. McDonald, H. Shahsavan, B. Zhao, *Macromolecular Materials and Engineering* **2014**, *299*, 237.
[77] T. Koerner, L. Brown, R. Xie, R. D. Oleschuk, *Sensors and Actuators B: Chemical* **2005**, *107*, 632.
[78] G. Shao, Z. C. Jiahao Wu, W. Wang, *Sensors and Actuators A* **2012**, *178*, 230.
[79] H. Hassanin, A. Mohammadkhania, K. Jiang, *Lab on a Chip* **2012**, *12*, 4160.
[80] C. Kumar, V. L. Houérou, T. Speck, H. F. Bohn, *Royal Society Open Science* **2018**, *5*, 172132.
[81] K. Koch, A. J. Schulte, A. Fischer, S. N. Gorb, W. Barthlott, *Bioinspiration & Biomimetics* **2008**, *3*, 046002.
[82] A. J. Schulte, K. Koch, M. Spaeth, W. Barthlott, *Acta Biomaterialia* **2009**, *5*, 1848.
[83] M. Sun, C. Luo, L. Xu, H. Ji, Q. Ouyang, D. Yu, Y. Chen, *Langmuir* **2005**, *21*, 8978.
[84] D. P. Pulsifer, A. Lakhtakia, *Bioinspiration & Biomimetics* **2011**, *6*, 031001.
[85] S.-M. Lee, T. H. Kwon, *Nanotechnology* **2006**, *17*, 3189.
[86] C. Poulard, F. Restagno, R. Weil, L. Léger, *Soft Matter* **2011**, *7*, 2543.
[87] V. Vaenkatesan, Z. Li, W.-P. Vellinga, W. H. de Jeu, *Polymer* **2006**, *47*, 8317.
[88] B. A. Krick, J. R. Vail, B. N. Persson, W. G. Sawyer, *Tribology Letters* **2012**, *45*, 185.
[89] V. Romero, E. Wandersman, G. Debregeas, A. Prevost, *Physical Review Letters* **2014**, *112*, 094301.
[90] E. Charrault, C. Gauthier, P. Marie, R. Schirrer, *Langmuir* **2009**, *25*, 5847.
[91] M. K. Chaudhury, G. M. Whitesides, *Langmuir* **1991**, *7*, 1013.
[92] Y. Morishita, H. Morita, D. Kaneko, M. Doi, *Langmuir* **2008**, *24*, 14059.
[93] P. Drechsler, W. Federle, *Journal of Comparative Physiology A* **2006**, *192*, 1213.

[94] J. M. R. Bullock, P. Drechsler, W. Federle, *The Journal of Experimental Biology* **2008**, *211*, 3333.
[95] F. Carrillo, S. Gupta, M. Balooch, S. J. Marshall, G. W. Marshall, L. Pruitt, C. M. Puttlitz, *Journal of Materials Research* **2005**, *20*, 2820.
[96] J. Nohava, N. Randall, N. Conté, *Journal of Materials Research* **2009**, *24*, 873.
[97] D. M. Ebenstein, L. A. Pruitt, *Nano Today* **2006**, *1*, 26.
[98] J. Greenwood, K. Johnson, *Philosophical Magazine A* **1981**, *43*, 697.
[99] S. Perutz, E. J. Kramer, J. Baney, C.-Y. Hui, C. Cohen, *Journal of Polymer Science, Part B: Polymer Physics* **1998**, *36*, 2129.
[100] E. K. Kroner, Adhesion Measurements on Patterned Elastomeric Surfaces, PhD Thesis, Doctoral dissertation, Saarländische Universitäts-und Landesbibliothek, **2011**.
[101] D. Grierson, E. Flater, R. Carpick, *Journal of Adhesion Science and Technology* **2005**, *19*, 291.
[102] K. Johnson, K. Kendall, A. Roberts, *Proceedings of the Royal Society of London. A. Mathematical and Physical Sciences* **1971**, *324*, 301.
[103] M. Deruelle, H. Hervet, G. Jandeau, L. Léger, *Journal of Adhesion Science and Technology* **1998**, *12*, 225.
[104] D. Maugis, *Journal of Colloid and Interface Science* **1992**, *150*, 243.
[105] R. G. Horn, J. N. Israelachvili, F. Pribac, *Journal of Colloid and Interface Science* **1986**, *115*, 480.
[106] E. Kroner, D. R. Paretkar, R. M. McMeeking, E. Arzt, *The Journal of Adhesion* **2011**, *87*, 447.
[107] D. Paretkar, M. Kamperman, A. S. Schneider, D. Martina, C. Creton, E. Arzt, *Materials Science and Engineering: C* **2011**, *31*, 1152.
[108] Y. Cao, D. Yang, W. Soboyejoy, *Journal of Materials Research* **2005**, *20*, 2004.
[109] L. Dorogin, A. Tiwari, C. Rotella, P. Mangiagalli, B. Persson, *Physical Review Letters* **2017**, *118*, 238001.
[110] K. Johnson, *Proceedings of the Royal Society of London A: Mathematical, Physical and Engineering Sciences* **1997**, *453*, 163.
[111] H. Hertz, J. Reine, *Journal of Applied Mathematics and Mechanics* **1882**, *92*, 156.
[112] J. Greenwood, J. P. Williamson, *Proceedings of the Royal Society of London. Series A. Mathematical and Physical Sciences* **1966**, *295*, 300.
[113] S. Gorb, M. Varenberg, A. Peressadko, J. Tuma, *Journal of the Royal Society Interface* **2007**, *4*, 271.
[114] G. Huber, S. N. Gorb, N. Hosoda, R. Spolenak, E. Arzt, *Acta Biomaterialia* **2007**, *3*, 607.
[115] C.-Y. Hui, N. Glassmaker, T. Tang, A. Jagota, *Journal of The Royal Society Interface* **2004**, *1*, 35.
[116] A. Mata, A. J. Fleischman, S. Roy, *Biomedical Microdevices* **2005**, *7*, 281.
[117] A. Ghatak, K. Vorvolakos, H. She, D. L. Malotky, M. K. Chaudhury, *Journal of Physical Chemistry B* **2000**, *104*, 4018.
[118] F. Schneider, J. Draheim, R. Kamberger, U. Wallrabe, *Sensors and Actuators A: Physical* **2009**, *151*, 95.
[119] N. Amouroux, L. Léger, *Langmuir* **2003**, *19*, 1396.
[120] M. Deruelle, M. Tirrell, Y. Marciano, H. Hervet, L. Léger, *Faraday Discussions* **1994**, *98*, 55.
[121] C. Neinhuis, H. G. Edelmann, *Journal of Microscopy* **1996**, *184*, 14.
[122] M. J. Talbot, R. G. White, *Plant Methods* **2013**, *9*, 36.
[123] R. Allen, G. David, *Zeitschrift fur wissenschaftliche Mikroskopie und mikroskopische Technik* **1969**, *69*, 193.
[124] E. Salmon, P. Tran, *Methods in Cell Biology* **2007**, *81*, 335.
[125] S. Gupta, F. Carrillo, C. Li, L. Pruitt, C. Puttlitz, *Materials Letters* **2007**, *61*, 448.

[126] E. Gacoin, C. Frétigny, A. Chateauminois, A. Perriot, E. Barthel, *Tribology Letters* **2006**, *21*, 245.
[127] W. Burger, M. J. Burge, *Digital Image Processing: An Algorithmic Introduction Using Java*, Springer, **2016**.

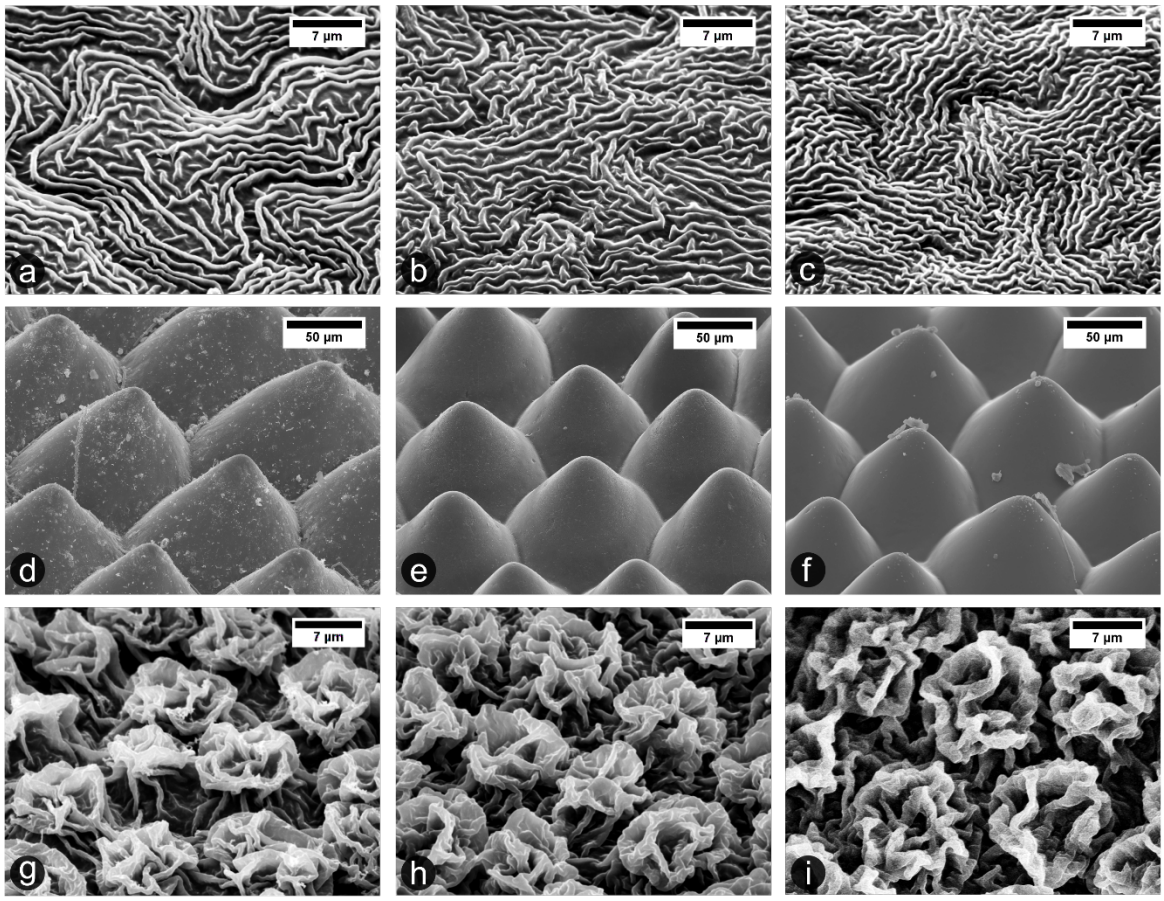

Figure 1. Scanning electron microscope images of original plant leaf surfaces (left column; a, d and g), their PDMS replicas (middle column; b, e and h), and respective PDMS replicas after n-heptane treatment (right column; c, f and i). (a-c) *Hevea brasiliensis* (adaxial, upper side surface) exhibits a micron-size wrinkled shape folds. (d-f) *Ludisia discolor* (adaxial, upper side surface) presents circular cone-like surfaces structures. (g-i) *Litchi chinensis* (abaxial, lower side surface) surface shows highly complex hierarchical structures.

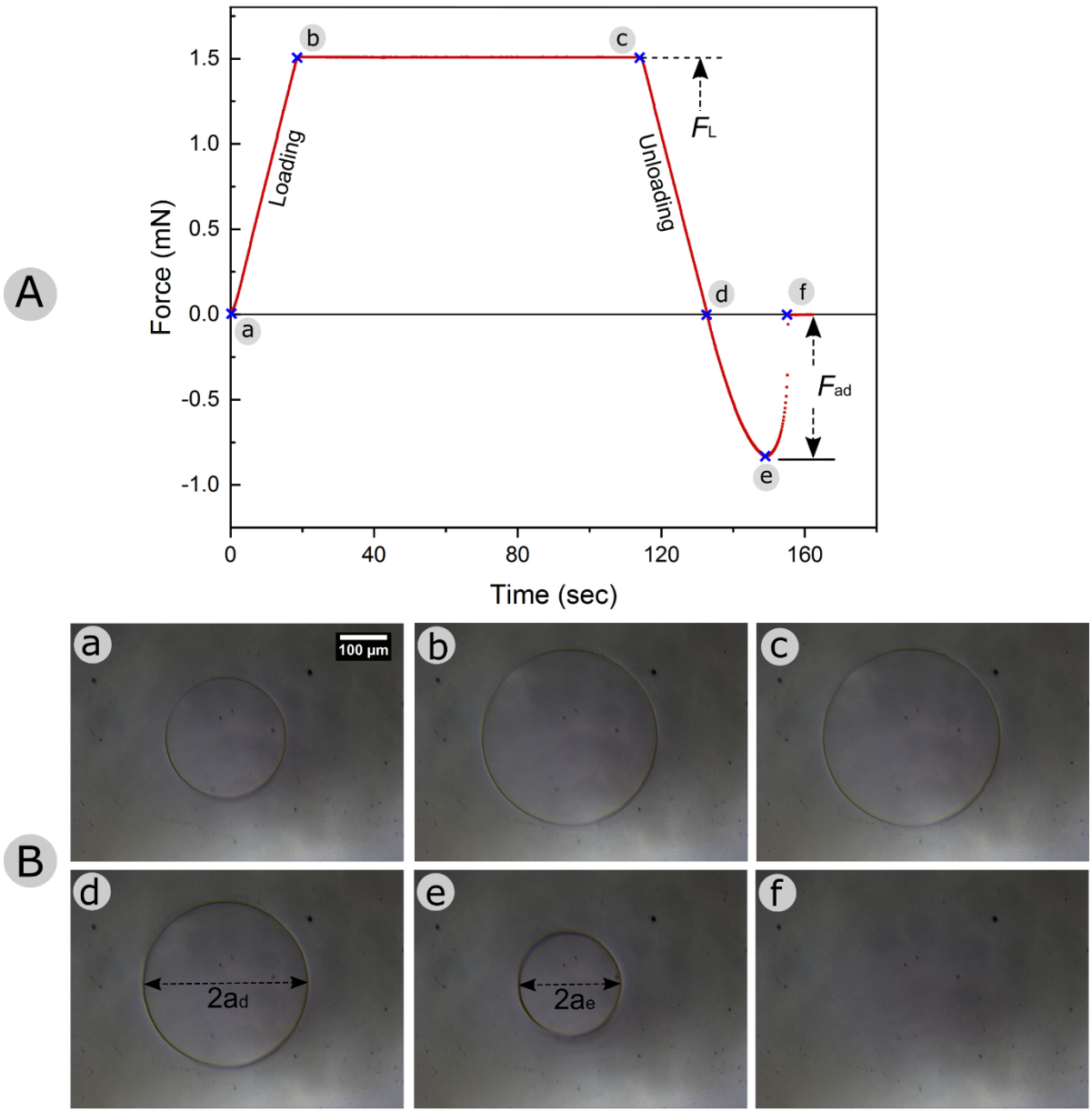

Figure 2. Graph (A) showing the force-time (displacement) curve for a whole test cycle on smooth PDMS sample, at a pre-load (F_L) of 1.5 mN. F_{ad} is the adhesion (pull-off) force recorded during the retraction step. Different points of interest (a-f) are marked on the curve. Phase a-b corresponds the loading step, b-c represents the relaxation step, c-d is the unloading phase. Phase d-e-f represents the retraction phase recording the adhesion pull-off force. In (B), a set of in-situ contact images (a-f) corresponding to the points marked on the force-displacement curve is shown. For the full *in-situ* video corresponding to the above images, see the supporting video 1 in supporting data. The scale bar in image 'a' holds for all the six images.

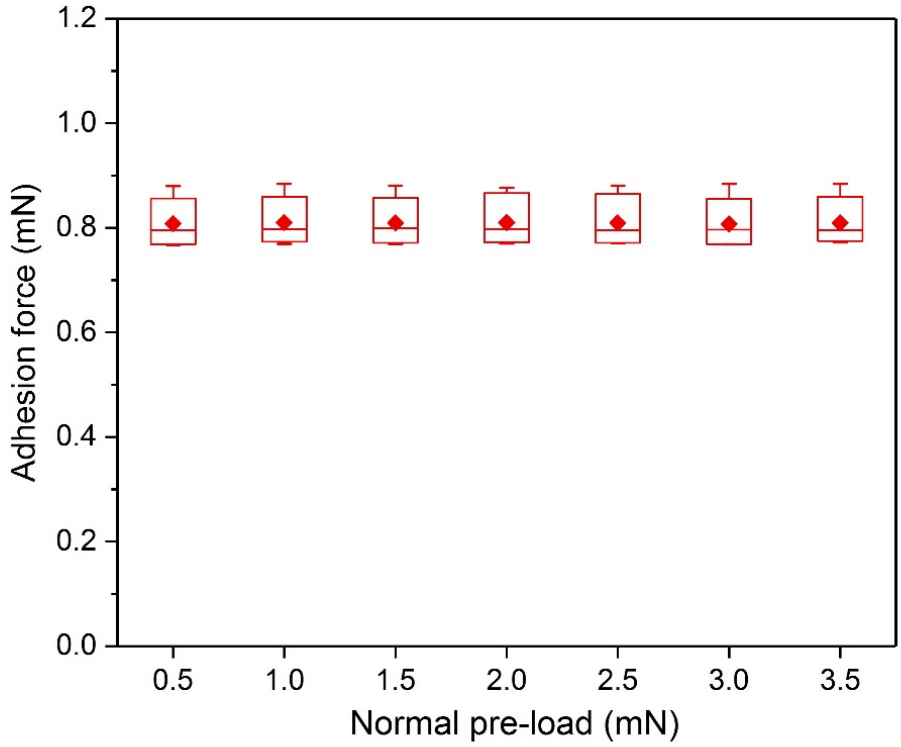

Figure 3. Plot of the variation of adhesive pull-off force (F_{ad}) with change in applied pre-load (F_L) for smooth PDMS sample. Data points are plotted as standard box-plot (25/75th percentile range) representing mean and median for N=7.

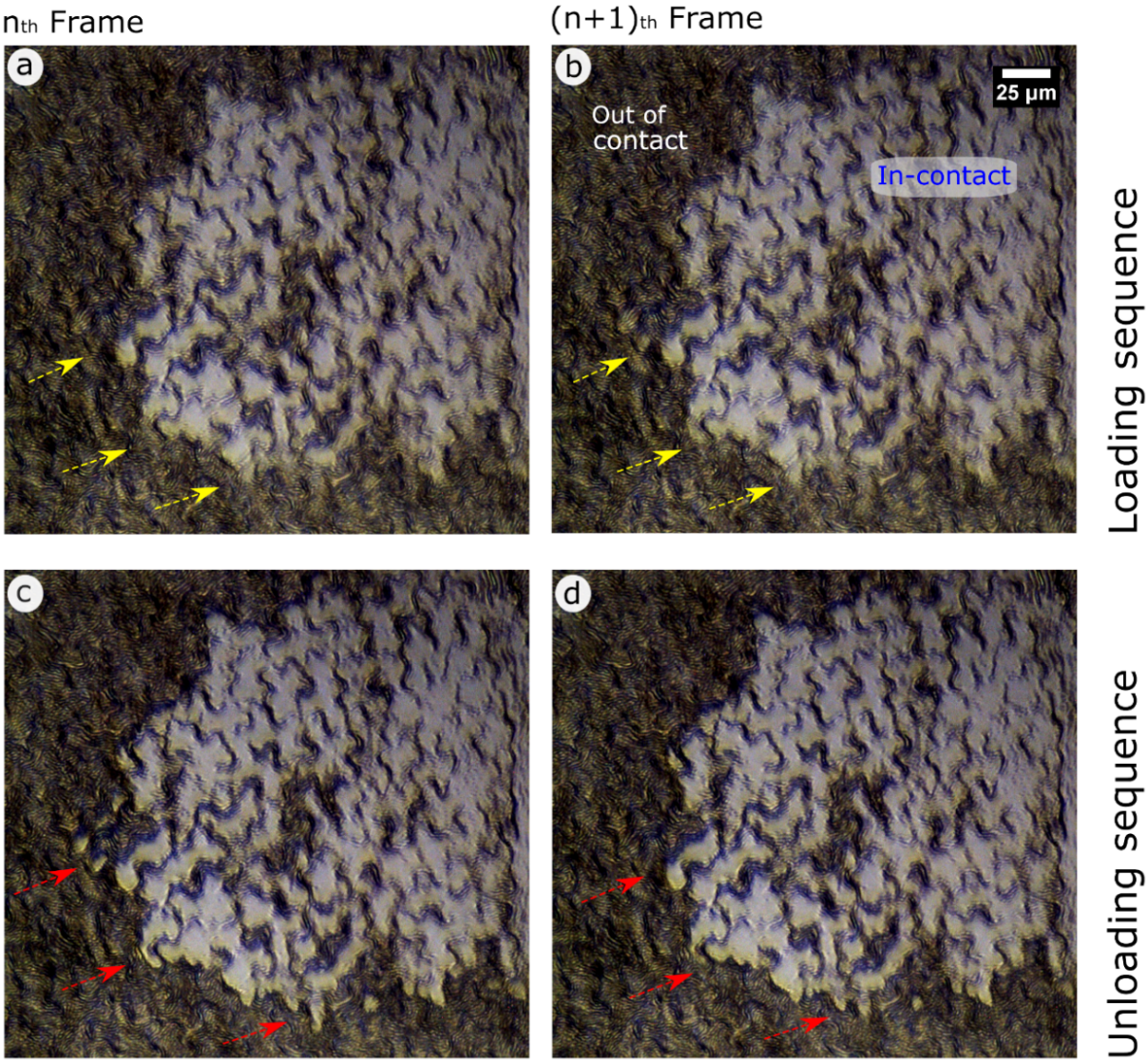

Figure 4. High magnification image sequence representing the contact formation behaviour during an attachment and detachment cycle. Bright areas represent the real area in contact. (a, b) shows the two consecutive (n_{th} and $(n+1)_{th}$) frames captured during the attachment (loading) cycle, and (c, d) during the detachment (unloading) cycle. The arrows are pointing to the areas of interest with distinct colour contacts at the edge for the attachment and detachment cycles. The scale bar in image b applies to all four images. A corresponding full video (Video 2) is provided in supporting data.

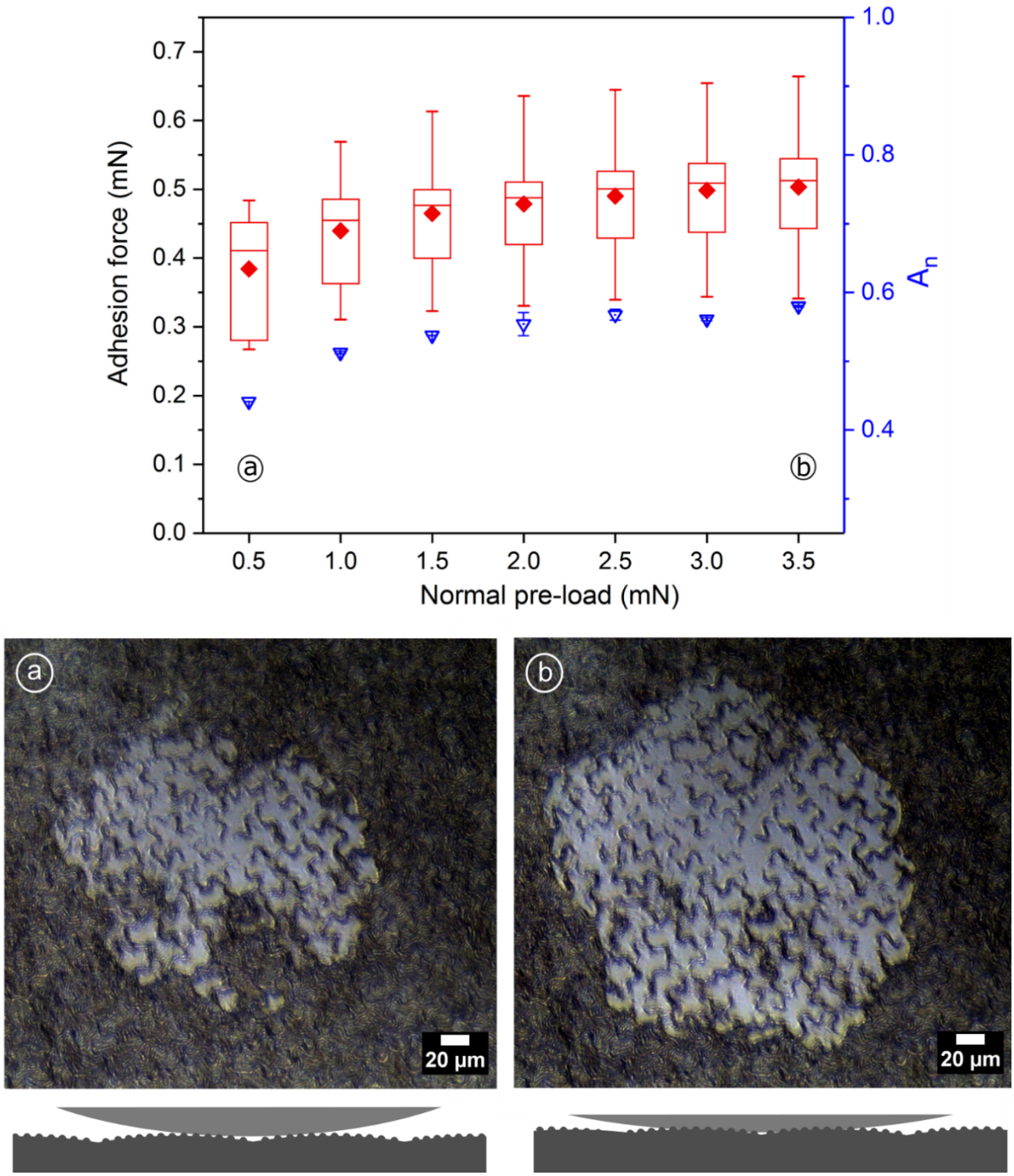

Figure 5. Upper part of the figure: Plot (in red, left-side ordinate) of the variation of adhesion pull-off force (F_{ad}) as a function of applied normal pre-load (F_L) for *Hevea* replica samples (N=6). Advancement of the normalized contact area (A_n) with increase in the pre-load (F_L), in blue on right-side ordinate. Lower part of the figure: Image I (for F_L= 0.5 mN) and image II (for F_L= 3.5 mN) show the *in-situ* contact areas at the absolute zero load condition, just before the retraction began.

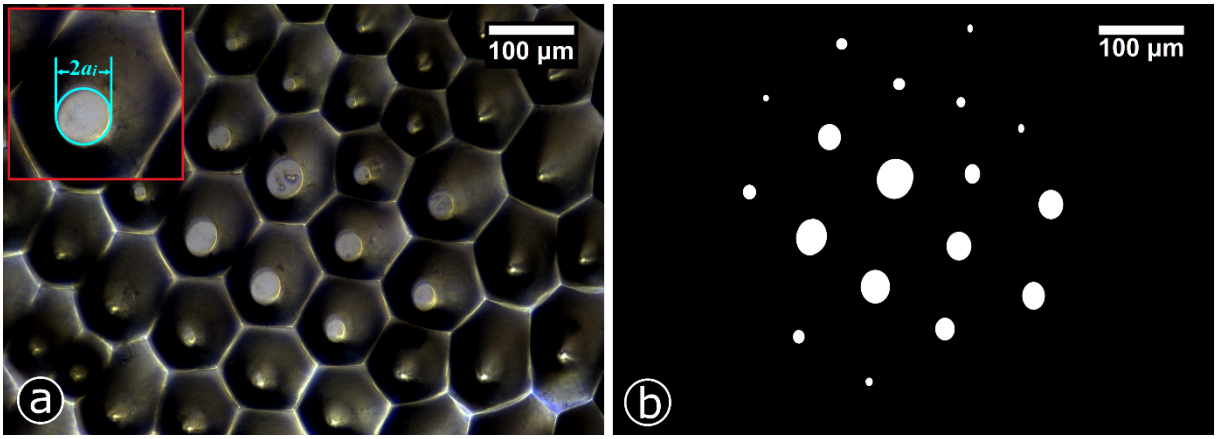

Figure 6. *In-situ* contact image for *Ludisia* replica at the full loading state for F_L = 1.5mN, clearly exhibiting the spatial distribution of micro-contact spots (a). Bright circular shaped spots on top of the conical structures represent the real contact area. The inset image in the upper left corner of the image indicates how the diameter (*2a*) of a real contact spot on top of a conical tip was estimated. (b) Shows the threshold image after image processing.

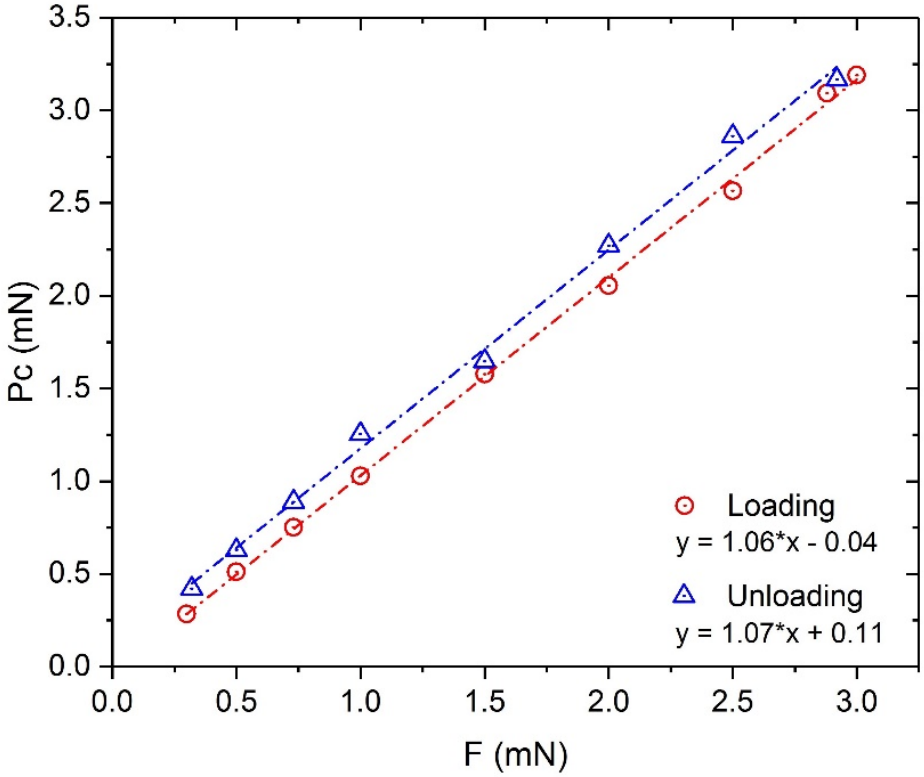

Figure 7. P_c versus F plot for the *Ludisia* replica surface. Linear slope and the overlapping of loading-unloading data points are validating the *Hertzian* contact theory locally. P_c= summation of inversely computed local normal loads, F= applied load.

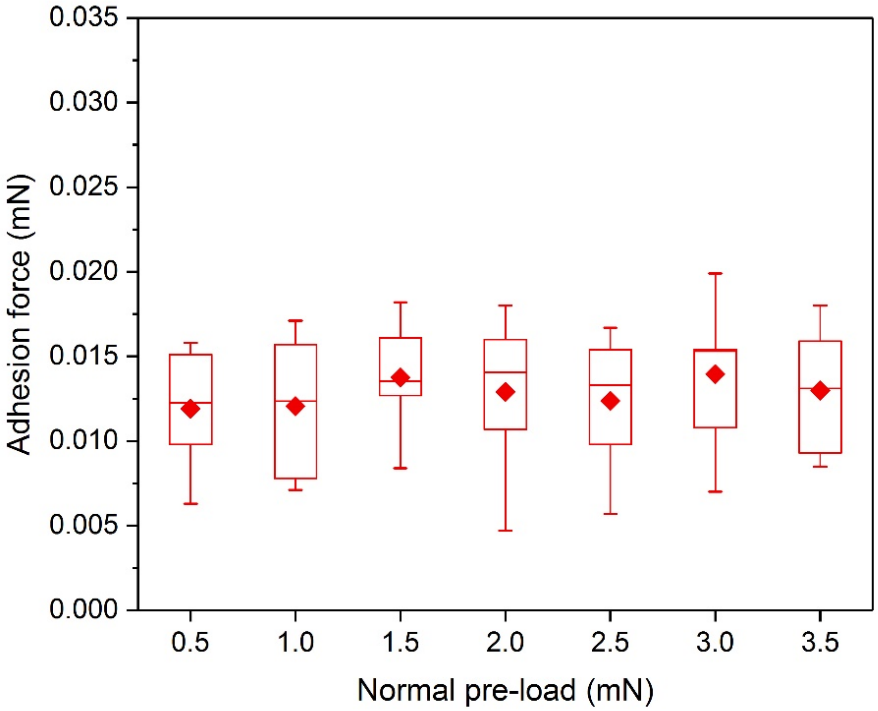

Figure 8. Variation in adhesion pull-off force (F_{ad}) with increasing applied normal pre-load (F_L) for *Ludisia* PDMS replicas, (N = 6).

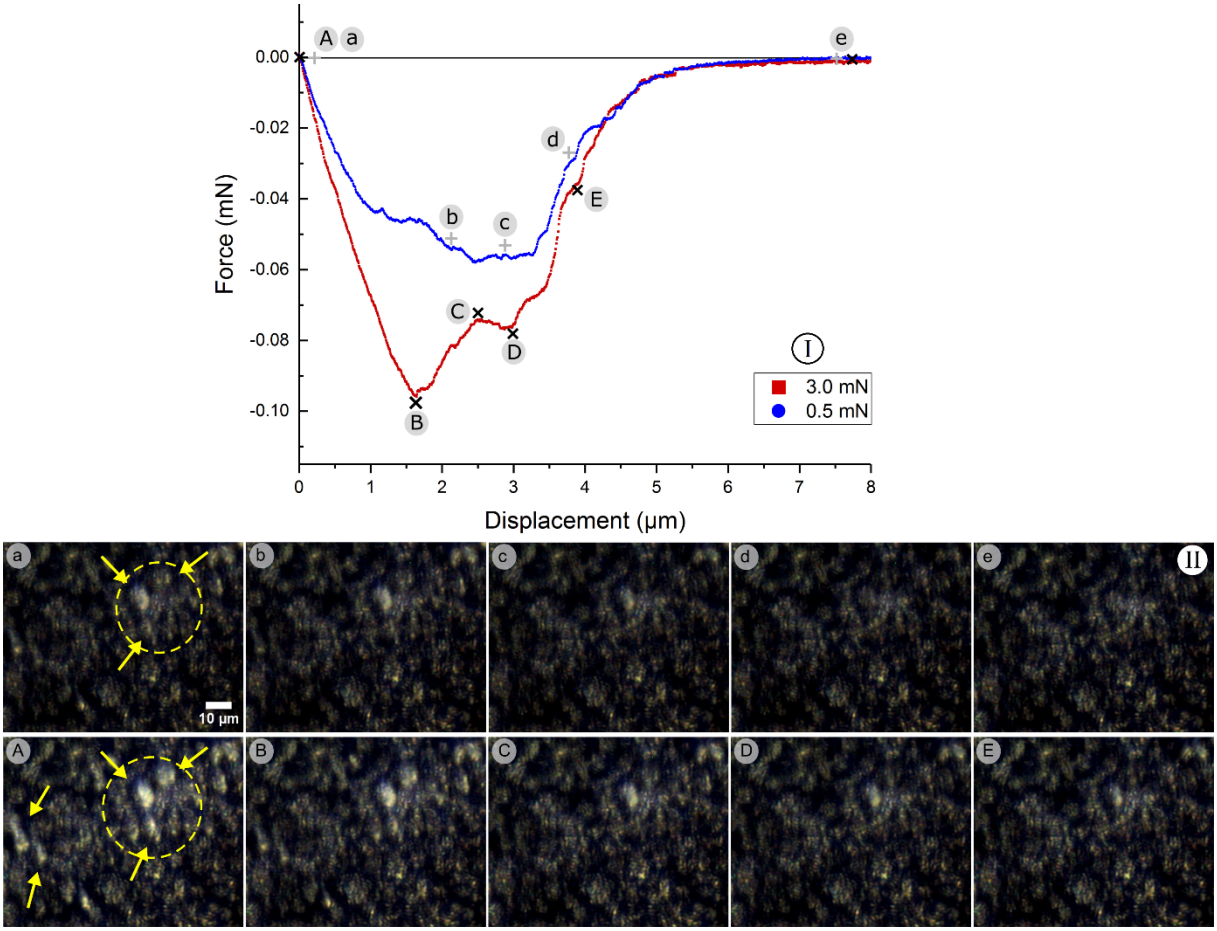

Figure 9. (I, upper part of the Figure) Diagram showing the retraction part of force-displacement curve for a *Litchi* replica sample, recorded at two different normal pre-loads, keeping all other parameters the

same. (II, lower part of the figure), (a-e) and (A-E) sequences of *in-situ* contact images at high magnification, corresponding to the points marked on force-displacement curves. Images with label 'a' and 'A' correspond to contact state at the absolute zero load during unloading, for pre-load F_L = 0.5 and 3.0 mN respectively. White arrows in image a and A are pointing towards the high contrast region exhibiting an agglomeration of a bunch of cuticular folds on individual epidermal cells (*rose flower shaped*). Images 'e' represent non-contact image, being the same for both pre-load values. The scale bar corresponds for all images is 10 µm. Corresponding full videos (Video 5 and Video 6) of both tests are given in supporting data.

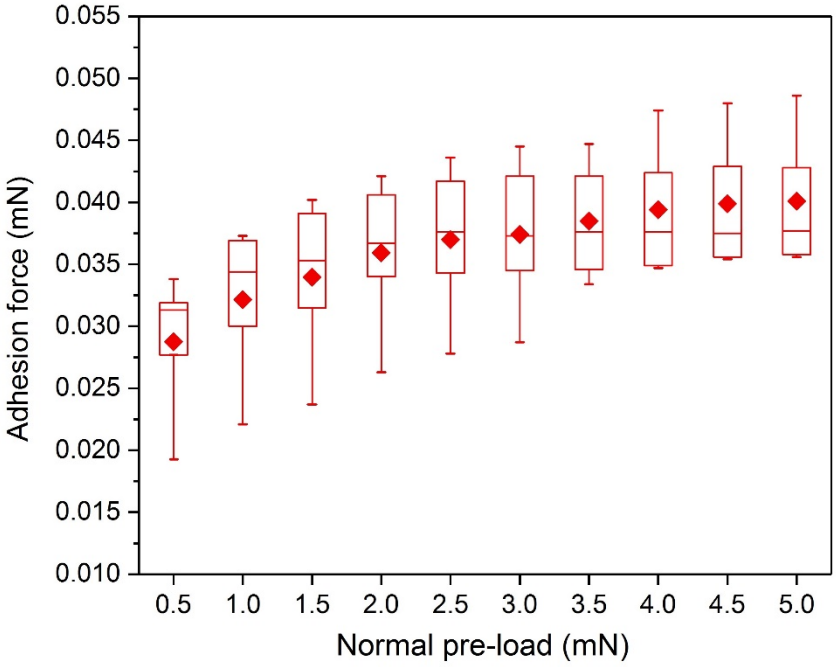

Figure 10. Plot of the variation of adhesion force (F_{ad}) with increasing applied normal pre-load (F_L) for *Litchi* replica samples, (N = 5). Plot shows an initial increase in F_{ad} which, however, gets saturated after 4.0 mN.

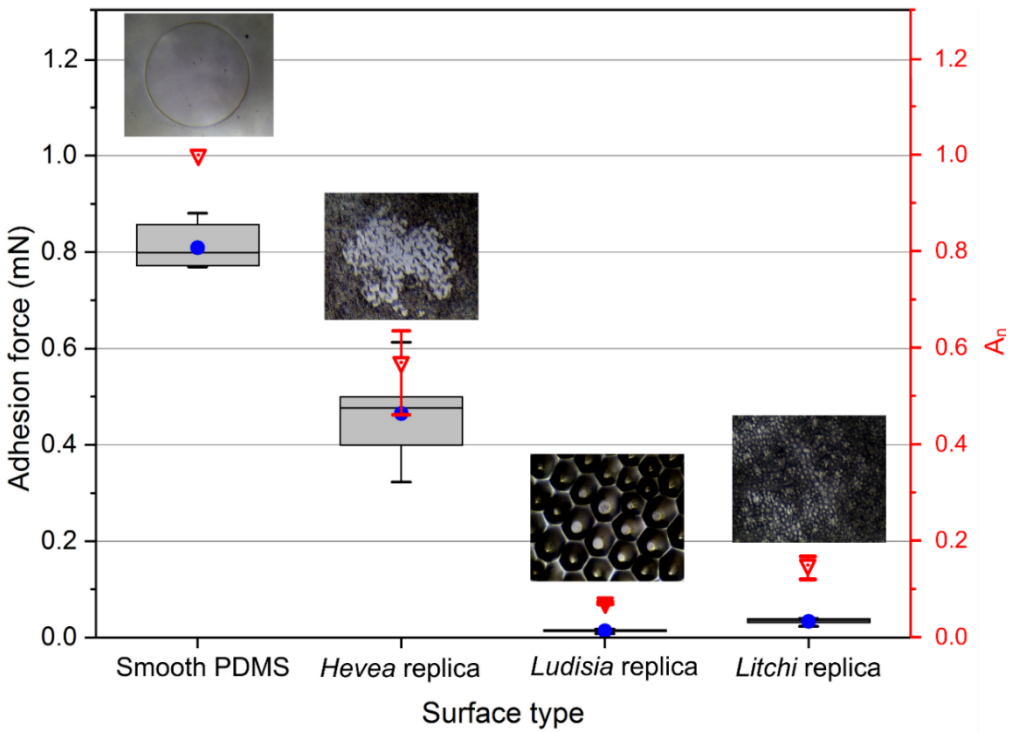

Figure 11. Overall comparison of adhesion pull-off force (F_{ad}) and normalized contact area (A_n) obtained for the four surfaces investigated, at a pre-load of 1.5 mN. Plot in blue (left-side ordinate) represents F_{ad} and plot in red (right-side ordinate) stands for A_n. Inserts show the representative real contact images under loading condition, for each surface type.

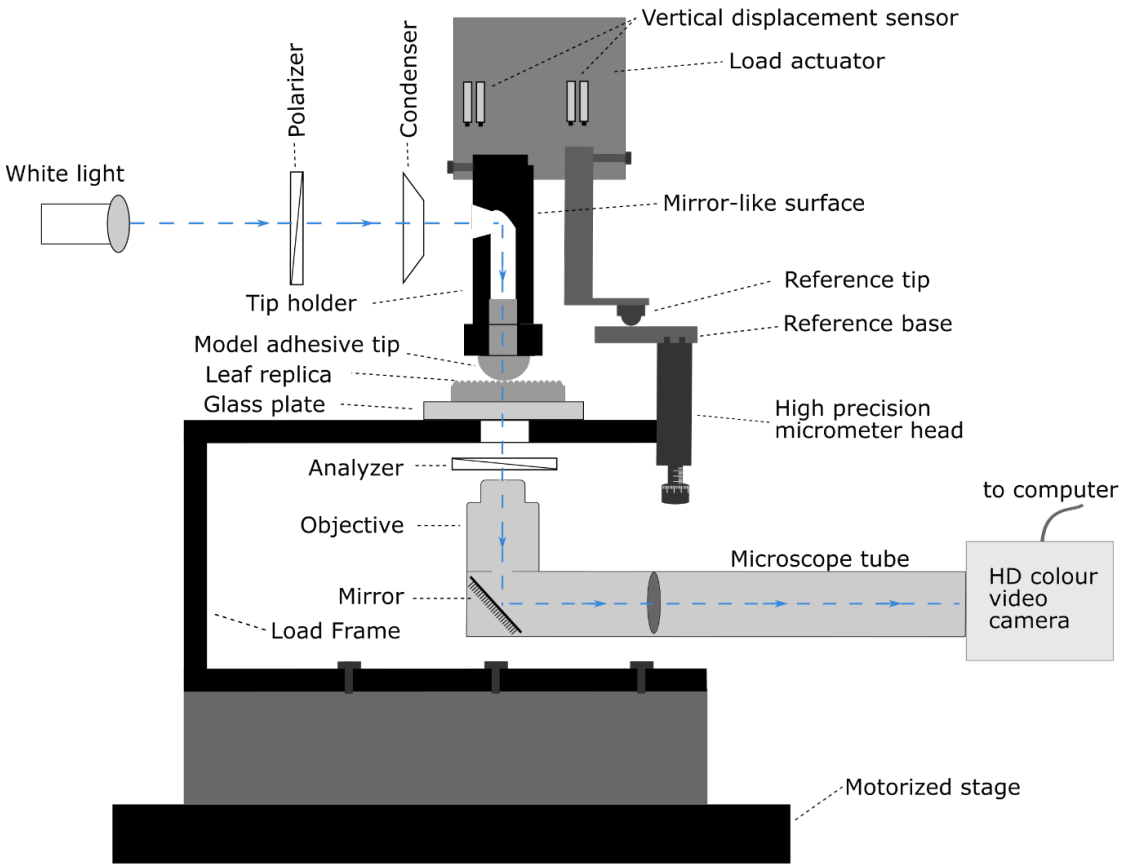

Figure 12. Simplified drawing of the modified ultra-nanoindenter setup for low-range adhesion force measurement in synchronization with *in-situ* contact visualization. The pull-off force measurement head is additionally equipped with a vertical displacement sensor and a reference tip to perform surface referencing. A white light was shined at the tip opening, passing through a polarizer and condenser lens. The light beam, after being reflected from an internal mirror-like surface bend toward the soft tip, is further transmitted through the real-contact junctions, appearing as high contrast bright spots in the recorded videos.

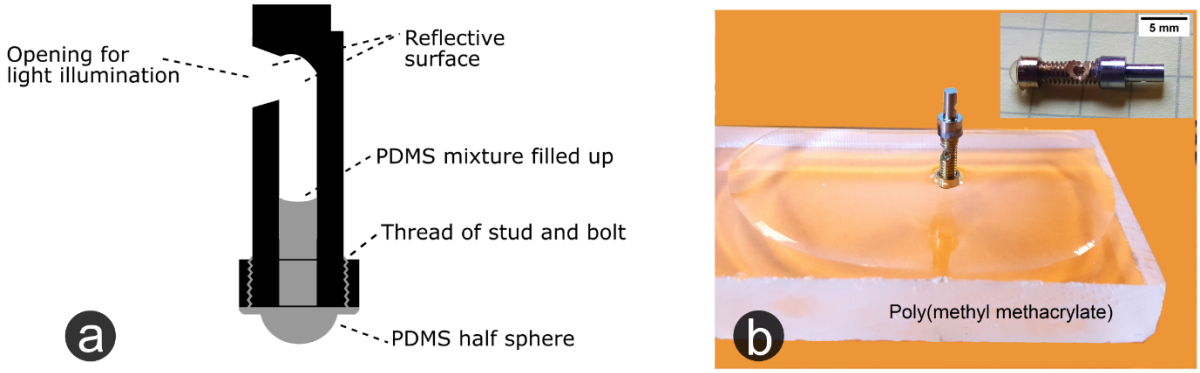

Figure 13. Simplified sketch of the tip assembly (a) showing that the PDMS tip is embedded within the tip assembly holder. (b) The PDMS liquid mixture filled up the hole due to capillary action, and a photograph of the resulting PDMS tip attached to the tip holder (in up-right corner of image b).

Adhesion mechanics investigation was carried on elastomeric replicas of natural leaf surfaces (decorated with complex hierarchical microstructures) using a modified ultra-nanoindenter equipped with an original *in-situ* real-contact visualization system. The study presents original insights on force-dependent adhesion behaviours associated to morphology dependent attachment-detachment modes, which may offer a valuable basis for designing bio-inspired functional surfaces.

Charchit Kumar[1,2,3], Damien Favier[2], Thomas Speck[1,3], and Vincent Le Houérou[2,4,*]

In-situ investigation of adhesion mechanisms on complex micro-structured biological surfaces